Article

Effects of Oxygen Content on Microstructure and Creep Property of Powder Metallurgy Superalloy

Yufeng Liu * , Shaorong Zhang , Lichong Zhang , Liang Zheng , Zhou Li , Lin Zhang , Guoqing Zhang

Posted Date: 25 March 2024

doi: 10.20944/preprints202403.1441.v1

Keywords: powder metallurgy superalloy; oxygen content; prior particle boundary; creep

Preprints.org (www.preprints.org) | NOT PEER-REVIEWED | Posted: 25 March 2024 doi:10.20944/preprints202403.1441.v1

Article

Effects of Oxygen Content on Microstructure and Creep Property of Powder Metallurgy Superalloy

Yufeng Liu [1,*], Shaorong Zhang [2], Lichong Zhang [1], Liang Zheng [1], Zhou Li [1], Lin Zhang [2] and Guoqing Zhang [1]

[1] Science and Technology on Advanced High Temperature Structural Materials Laboratory, AECC Beijing Institute of Aeronautical Materials, Beijing 100095, China; yufeng.liu@biam.ac.cn (Y. L.)
[2] University of Science and Technology Beijing 100083, China
* Correspondence: yufeng.liu@biam.ac.cn

Abstract: Effects of oxygen content on microstructure and creep property of FGH96 superalloy were investigated. When oxygen content increased from 135ppm to 341ppm, prior particle boundary (PPB) rose from degree 2 to degree 3, and the size of γ' phase on PPB enlarged from 1.07μm to 1.27μm, and MC carbide size grew from 77.4nm to 104.0nm. Meanwhile, the steady creep rate accelerated form 4.34×10^{-3} h^{-1} to 1.87×10^{-2} h^{-1}, and the creep rupture life shortened from 176h to 94h, and the creep rupture mode transferred from intergranular and transgranular mixed fracture to along PPB fracture. During creep, the micro-twins formation and gliding will be restrained by ∑3 boundaries. FGH96 superalloy with higher oxygen content contains less ∑3 boundaries and its micro-twins cross slipped instead of single direction slip in lower oxygen content superalloy. Consequently, specimen with higher oxygen content creeped faster and raptured earlier.

Keywords: powder metallurgy superalloy; oxygen content; prior particle boundary; creep

1. Introduction

Powder metallurgy (PM) nickel-based superalloy is wildly used on turbine disc and compressor disc of high-performance aero engine due to its fine grain size, uniform microstructure and excellent high temperature mechanical properties [1–4]. Hot isostatic pressing (HIPing) can completely densify the alloy powder, which is the key for powder metallurgy process to be applied to the preparation of rotating parts [5,6]. However, Prior Particle Boundary (PPB) easily formed during HIPing, which is consisting of carbide, oxide, carbon oxide and γ' phase, continuously or semi-continuously distributing along the boundary of the original powder particles [7,8]. Oxygen element adsorbed on the powder particle surface is considered to be the key for the formation of PPB, since Ti, Zr and other alloy elements of the nickel-based superalloy are easily to react with the oxygen element and form stable oxides. During HIPing, some of these oxides serve as nucleation and promote the precipitation of PPB.

The higher of the oxygen content of the powder is, the more PPB there will be, which deteriorates the microstructure integrity and mechanical properties. Rao et al. [12] studied the effect of oxygen content on the microstructure and mechanical properties of HIPed Inconel718 alloy, and found that PPB especially existed in alloy with high oxygen content. The increase of oxygen content inhibited the formation of recrystallization and annealing twins, which would sharply impair the high temperature plasticity and fracture toughness, although had little effect on the yield strength and tensile strength. He et al. [13] studied the effect of powder making process on the microstructure and thermal deformation behavior of PM nickel-based superalloy. Results show that compared with plasma rotating electrode method, the powder prepared by argon gas atomization formed more PPB at HIPing due to its higher oxygen content, and was more likely to crack during subsequent thermal deformation. MacDonald et al. [14] studied the effect of powder characteristics on the microstructure and mechanical properties of HIPed CM247LC nickel-based superalloy, and found that the alloy prepared by coarse powder had lower oxygen content and more ∑3 grain boundary, which improved the high temperature properties.

Nevertheless, few relevant studies on the influence of oxygen content on creep property of PM nickel-based superalloy. Creep performance is an important factor for structural design and life evaluation for aeroengine [15–17]. Therefore, it is necessary to study the effect of oxygen content on microstructure and creep property of PM nickel-based superalloy.

2. Materials and Methods

2.1. Alloys and Preparation

FGH96 superalloy studied in this paper is suitable for the fabrication of the turbine disc operating at temperatures below 750 °C. The prealloying powder was obtained by vacuum induction melting argon gas atomization (VIGA) and sieved into less than 63μm. For comparation, part of the powder was preoxidized by a heating furnace at 200 °C for 5 hours, simulating the heating process that may occur for the high-frequency vibration during sieving in industrial production.

The original and preoxidized FGH96 superalloy powder were respectively loaded in a stainless-steel bucket with 160 mm in diameter and 200 mm in height. Then degassing was carried out at 450 ℃ under below 1.0×10^{-3} Pa for 8 hours, followed by encapsulating to prevent air from flowing to these buckets. Finally, the two buckets were HIPed at 1170 ºC under 140 MPa for 4 hours to get fully densified superalloy with two different oxygen content.

2.2. Materials Characterization

The oxygen content of the powder and HIPed FGH96 superalloy were detected by pulse heating-infrared absorption method with an oxygen and nitrogen analyzer (TC600, LECO, SAN Jose, America) and the results were displayed in Table 1.

Table 1. Oxygen content of superalloy under different state (ppm).

State	Original	Preoxidized
Powder	141	397
HIPed	135	341

To investigate the effect of oxygen content on microstructure of the FGH96 superalloy, the samples were ground and mechanical polished for PPB evaluation. For EBSD analysis, these polished sample should be electro-polished a step further in a solution composed of 20ml HCl + 80ml CH_3OH under the voltage of 25V for 15s. And for phases observation by SEM, these electro-polished samples should be electro-etched in a 170ml H_3PO_4 + 10ml H_2SO_4 + 15g CrO_3 solution under the voltage of 5V for 2-3s. The PPB degree was estimated with metallographic microscopy (OM, DM8000M, LEICA, Witzler, Germany). The γ' phase and carbon morphology were captured using the field emission scanning electron microscope (FE-SEM, Regulus8100, HITACHI, Tokyo, Japan) under back scattering electron mode (BSE). And crystal orientation images, grain size and grain boundary distributions were obtained by electron back scattering diffraction mode (EBSD). The average size and proportion of γ' phase and carbon were measured by Image-Pro Plus analysis software. The phases crystal structure and annealing twin were analyzed with field emission transmission electron microscope (TEM, Tecnai G2 F20, FEI, Hillsboro, America).

To reveal the influence of oxygen content on creep property of FGH96 superalloy, the creep experiment at 700 ºC under 690 MPa was carried out on a electronic creep testing machine (RDL100, SINOTEST, Changchun, China). The fracture morphology was observed by SEM under secondary electron (SE) mode and the local misorientation maps before and after creep experiment were obtained by SEM under EBSD mode. The annealing twin before and after creep experiment were also analyzed with TEM.

3. Results and Discussion

3.1. Effect of Oxygen Content on Microstructure of FGH96 Superalloy

Figure 1 is the mechanical polished morphology of FGH96 superalloy with different oxygen content, indicating clear spherical original powder particle boundary. According to the PPB grade evaluation principle given by Ingesten et al. [18], the PPB grades of FGH96 superalloy with oxygen content of 135ppm and 341ppm are grade 2 and grade 3 respectively. In a word, the higher the oxygen content is, the more continuously the PPB will be.

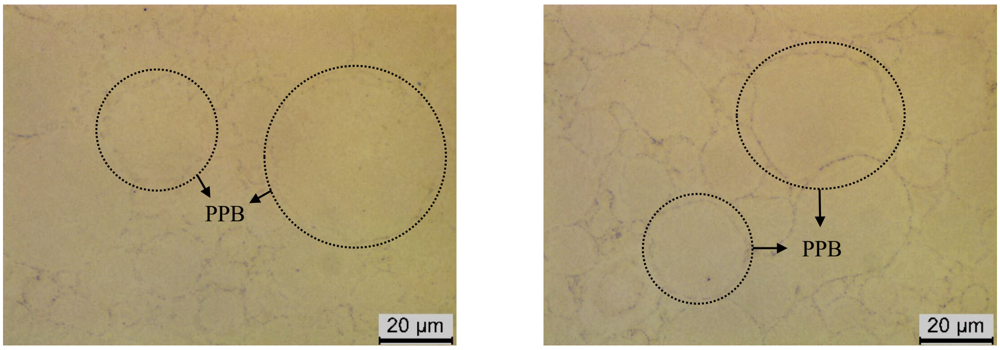

(**a**) (**b**)

Figure 1. OM images of FGH96 superalloy with different oxygen content: (a)135ppm, (b)341ppm.

The phase composition of FGH96 superalloy with different oxygen content is mainly γ matrix, γ′ phase and carbide. The γ′ phase can be divided into three types: one is irregular long strips or large blocks (Figure 2a,b, marked γ'_1), which distributes at PPB; and the second is petal-like or spherical (Figure 2c,d, marked γ'_2), which disperses inside the PPB; and the third is small spherical (Figure 2c,d, marked γ'_3), precipitating between γ'_2 phases. Quantitative metallography demonstrated the effect of oxygen content on γ′ phase size and the results are displayed in Table 2. It is clear that the oxygen content has great influence on the γ'_1 phase size, which of the FGH96 superalloy with oxygen content of 341ppm increases by 20% compared with that of 135ppm. Yet, the size of γ'_2 and γ'_3 phases rarely affect by oxygen content, the γ'_2 phase size of the superalloy with oxygen content of 135ppm and 341ppm are 325.4nm and 320.7nm respectively, while the γ'_3 phase size are 22.6nm and 24.8nm respectively.

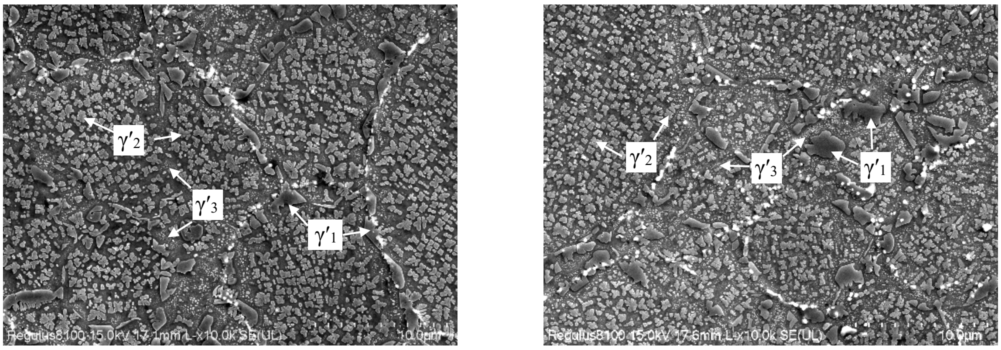

(**a**) (**b**)

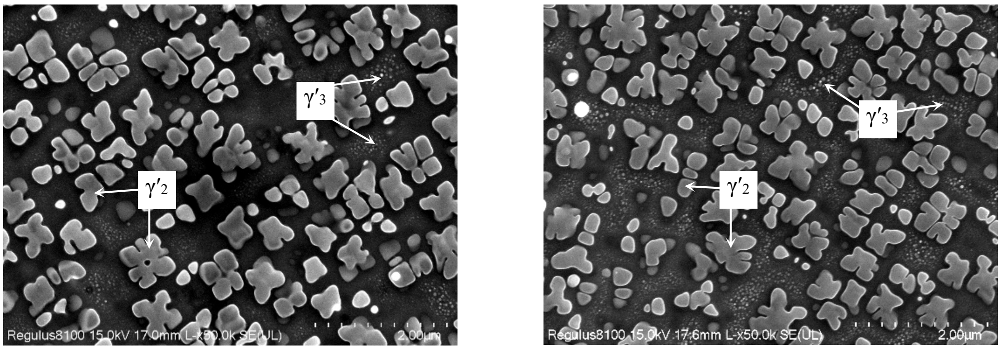

(c) (d)

Figure 2. γ′ phase morphology of FGH96 superalloy with different oxygen content: (a, c) 135ppm, (b, d) 341ppm.

Table 2. γ′ phase size of FGH96 alloy with different oxygen content.

Oxygen content / ppm	**γ'_1 / μm**	**γ'_2 / nm**	**γ'_3 / nm**
135	1.07	325.4	22.6
341	1.27	320.7	24.8

From the SEM-BSE images in Figure 3a,b, carbide in FGH96 superalloy with different oxygen content has two forms, that is MC carbide with black contrast and $M_{23}C_6$ carbide with white contrast, both of which are scattered among PPB. Corresponding selected area electron diffraction patterns (SAED) are shown in Figure 3c,d, which is consistent with the results of reference [19]. The average size and percentage of these two kinds of carbides were statistically analyzed and the results are displayed in Figure 3. When oxygen content increases from 135ppm to 341ppm, the size of MC carbide increased from 77.4nm to 104.1nm and the percentage rises from 0.15% to 0.22%. Therefore, oxygen around powder particle surface accelerates the precipitation and growth of MC carbide. However, oxygen content has little influence on the precipitation of $M_{23}C_6$ carbide. The average sizes of $M_{23}C_6$ carbide in FGH96 superalloy with oxygen content of 135ppm and 341ppm are 768.9nm and 824.3nm respectively, and the percentages are 0.10% and 0.11% respectively.

In comparison with the original superalloy powder, Ni, Ti, Cr, Al and other elements on the surface of the peroxidized powder oxidized more seriously, forming a thicker oxide layer as well as a broader alloy elements deletion region [20]. In consequence, weaker driving force of γ′ phase precipitation and mutual resistance of growing up around powder particle surface during HIPing, resulting in bigger γ'_1 phase than γ'_2 phase, and larger average size of γ'_1 phase in FGH96 superalloy with higher oxygen content than that with lower oxygen content. Since the internal chemical state of the powder nearly unaffected by surface oxidation, γ'_2 and γ'_3 phase in different oxygen content superalloy presented almost the same morphology and average size. Meanwhile, a thicker oxide layer means more tiny oxide particles around the powder surface, tending to form more and bigger MC carbide at PPB.

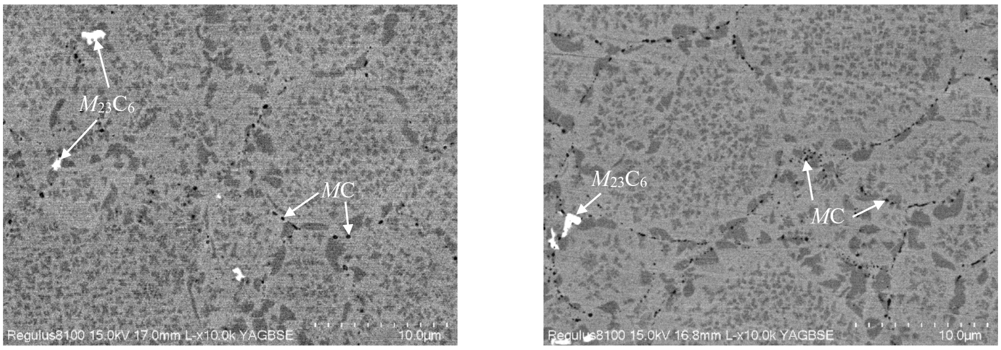

(**a**) (**b**)

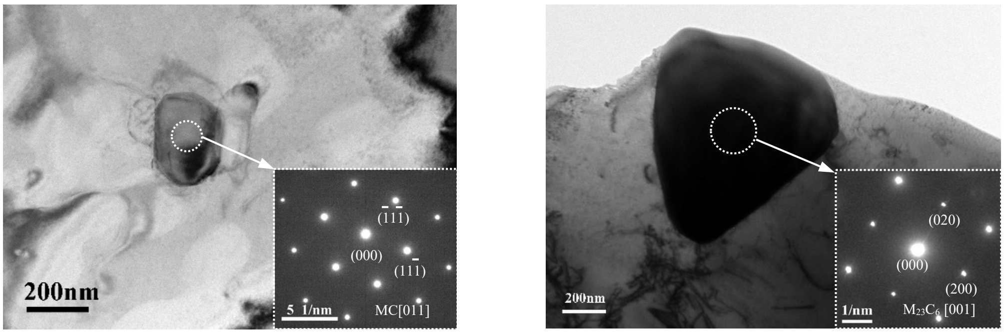

(c) (d)

Figure 3. SEM-BSE images of FGH96 superalloy with (a)135ppm, (b)341ppm oxygen content and SAED patterns of (c) MC and (d) $M_{23}C_6$ carbides.

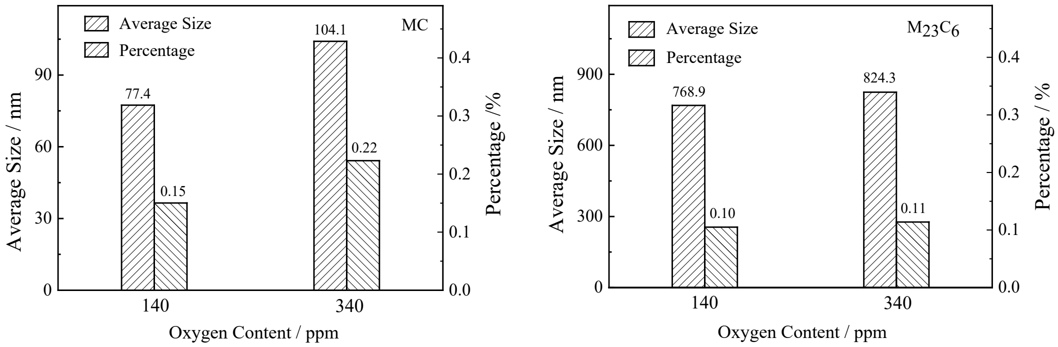

(**a**) (**b**)

Figure 4. Histograms of carbide average size and percentage in FGH96 superalloy: (a) MC carbide, (b) $M_{23}C_6$ carbide.

The effect of oxygen content on crystal orientation and grain size distribution of FGH96 superalloy was studied by EBSD. Figure 5a,b illustrate the crystal orientation graphs of FGH96 superalloy with oxygen content of 135ppm and 341ppm respectively. Each crystal orientation is random, implying the isotropous microstructure and oxygen content has no significant effect on the crystal orientation. But the grain size distribution changes significantly with the increase of oxygen content. According to the grain size distribution diagrams in Figure 6a,b, the maximum grain size of superalloy with oxygen content of 341ppm is 10μm larger than that of 135ppm, while the average grain size is smaller by 40%. Because the FGH96 superalloy with higher oxygen content has more fine grains mainly gathering around PPB, and the proportion of grains less than 2μm is about 80% and 62% and in superalloy with oxygen content of 341ppm and 135ppm respectively. As a result, with the increase of oxygen content, the grain size distribution range become broader, but the average grain size is smaller.

The grain size distribution has strong relation to the degree of plastic deformation and recrystallization process during HIPing. The shear stress exerted by the external gas densifies the powder particles with drastic plastic deformation at the very beginning of HIPing. While the densified material tends to annealing in the following holding and cooling stage. Higher oxygen content of the powder tends to precipitate more oxides and carbides, which will hinder the deformation of the powder particles and grain growth [12]. Therefore, under the same HIPing condition, the powder with higher oxygen content formed more continuous PPB, lowering the degree of plastic deformation, so the original large grain size of the powder was retained, and many fine recrystallization grains also reserved owing to the insufficient driving force to grow up.

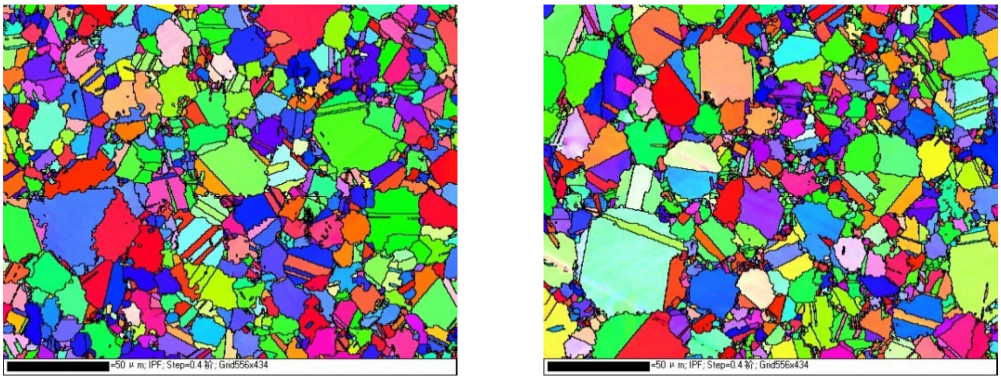

(**a**) (**b**)

Figure 5. Crystal orientation images of FGH96 superalloy with different oxygen content: (a) 135ppm, (b) 341ppm.

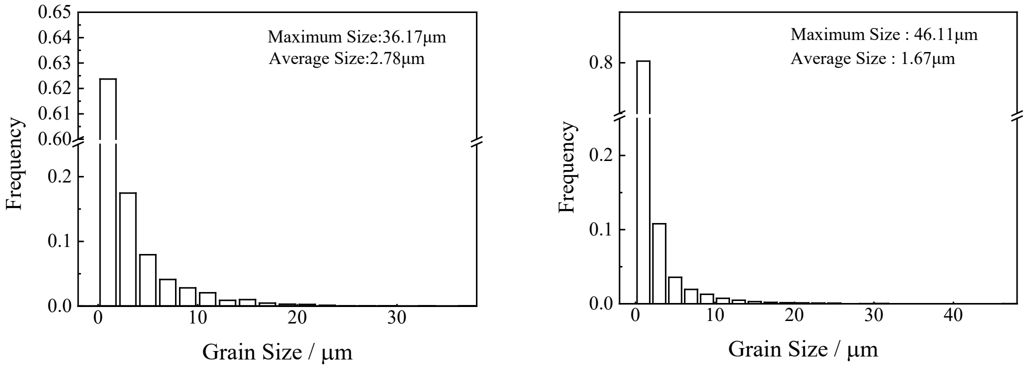

(**a**) (**b**)

Figure 6. Grain size distribution of FGH96 superalloy with different oxygen content: (a) 135ppm, (b) 341ppm.

Figure 7 is the histogram of grain boundary distribution, and when the oxygen content increases from 135ppm to 341ppm, the twin boundary (60°), ∑3, of FGH96 alloy decreases from 34% to 30%, and the small angle boundary (< 10°) increases from 12% to 17%. Figure 8 shows the ∑3 boundary distribution maps of superalloy with different oxygen content. Similar to many FCC structure alloys [21], due to the low-level fault energy and large deformation during HIPing, a large number of annealing twins formed. As described above, higher oxygen content superalloy deforms harder during HIPing and fine recrystallized grains are difficult to grow, so more small angle grain boundary reserved.

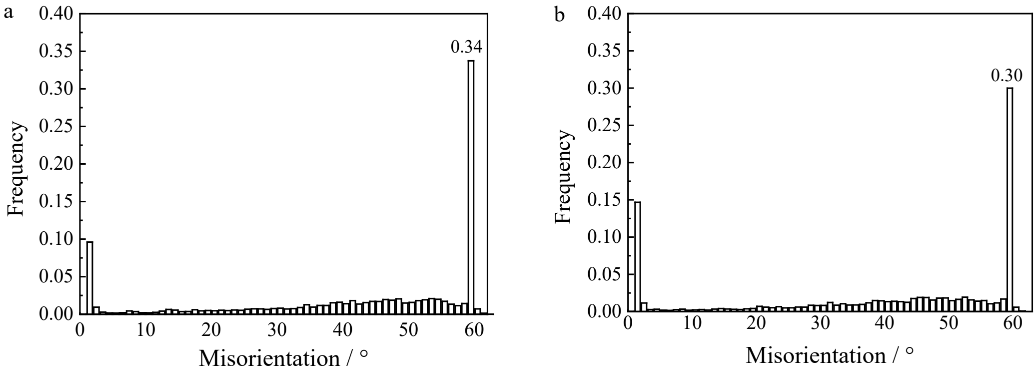

(**a**) (**b**)

Figure 7. Grain boundary distribution of FGH96 superalloy with different oxygen content: (a) 135ppm, (b) 341ppm.

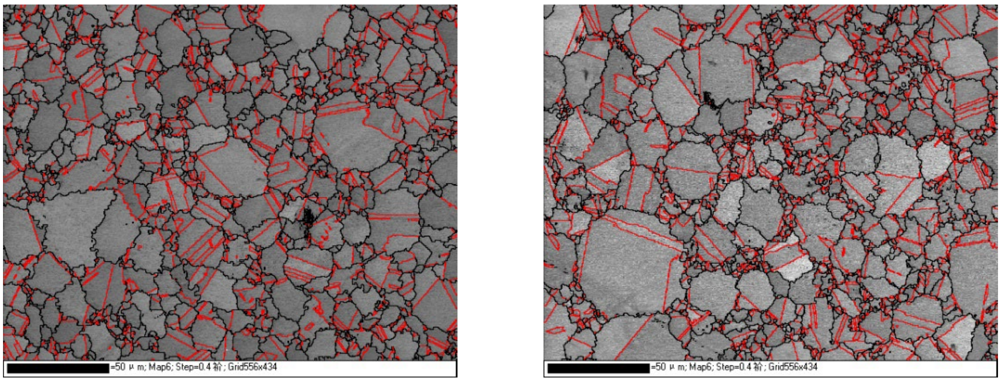

(**a**) (**b**)

Figure 8. Twin boundaries of FGH96 superalloy with different oxygen content: (a) 135ppm, (b) 341ppm.

3.2. Effect of Oxygen Content on Creep Property of FGH96 Superalloy

The creep curves of FGH96 superalloy with different oxygen content at 700 °C and 690 MPa have three stages, creep transition stage (I), steady creep stage (II) and creep acceleration stage (III) in Figure. 9, and the latter two stages domains. When the oxygen content increases from 135ppm to 341ppm, the duration of the steady creep stage decreases from 43 hours to 21 hours, and the steady creep rate changes from 4.34×10^{-3} h^{-1} to 1.87×10^{-2} h^{-1}, and the creep life diminishes from 176h to 94h, and the total strain shortens from 13.9% to 8.5%.

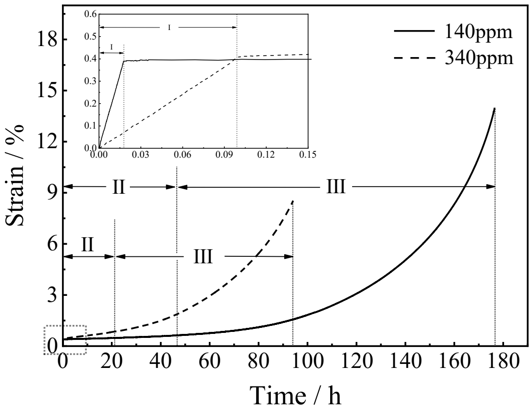

Figure 9. Creep curves of FGH96 superalloy with different oxygen content.

The creep fracture morphology of the specimen with oxygen content of 135ppm contains three typical regions, namely fracture source region, crack extension region and shear lip region, as shown in Figure 10a region I, II and III respectively. The crack originated at the edge of the specimen, and gradually expanded inward, and then tore rapidly. Figure 10b is the fracture source region, where a small number of PPB can be found. Wedge-shaped cracks can be seen from the enlarged image of the rectangular area in Figure 10b, indicating the intergranular and transgranular mixed fracture. Figure 10c displays the crack extension region, where there is a large number of deep dimples, implying transgranular fracture feature, and a few PPB. Figure. 10d is the shear lip region, in which a large number of shallow dimples exists.

The creep fracture morphology of the specimen with oxygen content of 341ppm also has these three typical regions, showing in Figure 11a region I, II and III respectively. A large quantity of PPB appears in both the fracture source region and the crack extension region (Figure 11b,c), indicating that the crack originated at the PPB and also expanded along PPB. No secondary cracks were found in the whole fracture, meaning that the crack extended fast compared with the lower oxygen content creep specimen, which confirms with the creep curves. The shear lip region (Figure 10a region III) is relatively small compared with that of lower oxygen content (Figure 11a region III), and the shallow dimples can also be observed in Figure 11d.

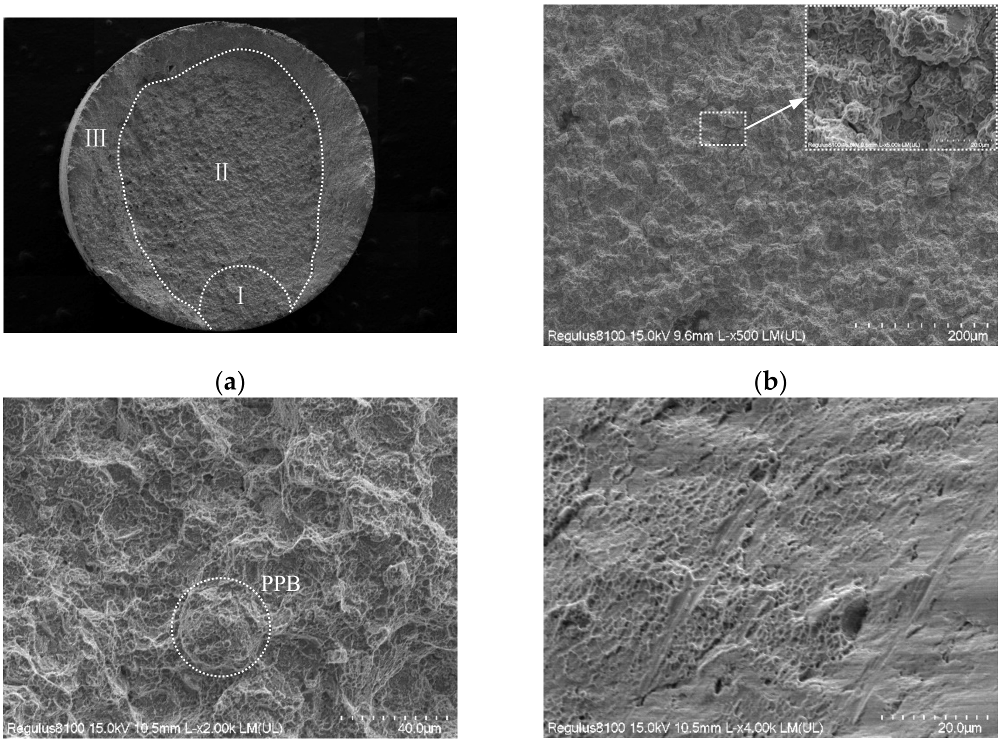

(**a**) (**b**)

(c) (d)

Figure 10. Creep fracture morphology specimen with 135ppm oxygen content: (a) overall fracture morphology, magnified image of region (b) I, (c) II, (d) III in (a).

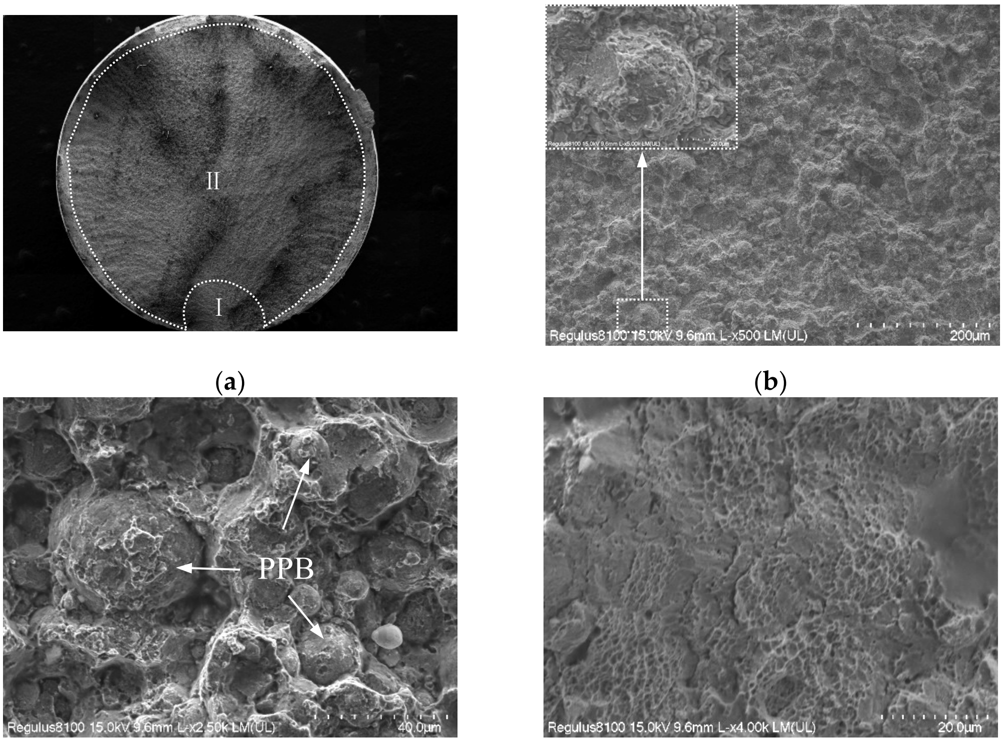

(**a**) (**b**)

(c) (d)

Figure 11. Creep fracture morphology specimen with 341ppm oxygen content: (a) overall fracture morphology, magnified image of region (b) I, (c) II, (d) III in (a).

The local misorientation distribution curves of the specimens with different oxygen content before and after creep experiment demonstrate in Figure 12. There is no significant difference between the two local misorientation distribution curves before creep. However, after creep test, the two local misorientation distribution curves dramatically changed, which indicates large strain occurred in these two specimens during creep test. Compared with the creep specimen with oxygen content of 341ppm, the specimen with that of 135ppm has a broader local misorientation distribution, which means a larger strain during creep, and as a result, it has a longer creep life, regarding its lower crack extension rate.

The local misorientation maps of the specimens with two different oxygen content before and after creep experiment illustrate in Figure 13. Before creep test, the two local misorientation maps exhibit uniform distribution. While after creep, the stain of the specimen with oxygen content of 135ppm clusters on grain boundaries and in fine grains, but the stain of the specimen with oxygen content of 341ppm gather around PPB. Therefore, when the oxygen content increases from 135ppm to 341ppm, the creep fracture changes from intergranular and transgranular mixed fracture to PPB fracture.

During creep, specimen releases stress concentration by the grain deformation and recrystallization. As analyzed above, deformation was resisted by the continuous PPB networks and much fine recrystallization grains formed around PPB in FGH96 superalloy with oxygen content of 341ppm, thus the strain concentrated along PPB, becoming crack origin and extension path.

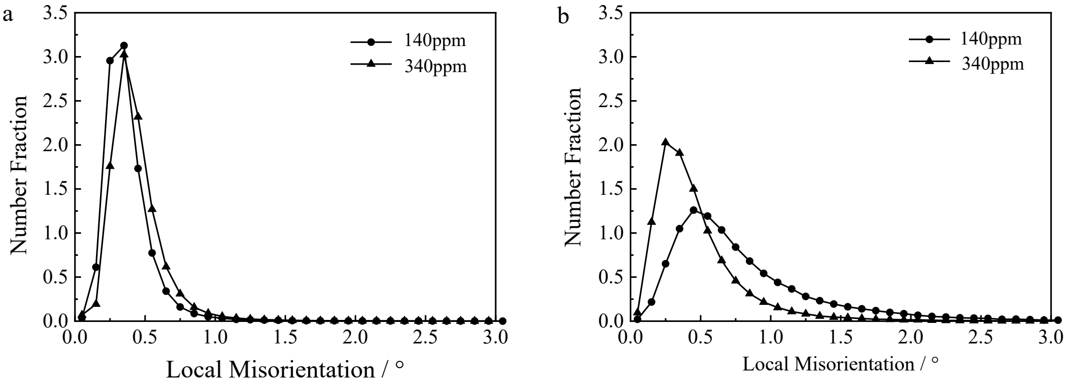

(a)

(b)

Figure 12. Local misorientation distribution: (a) before creep, (b) after creep.

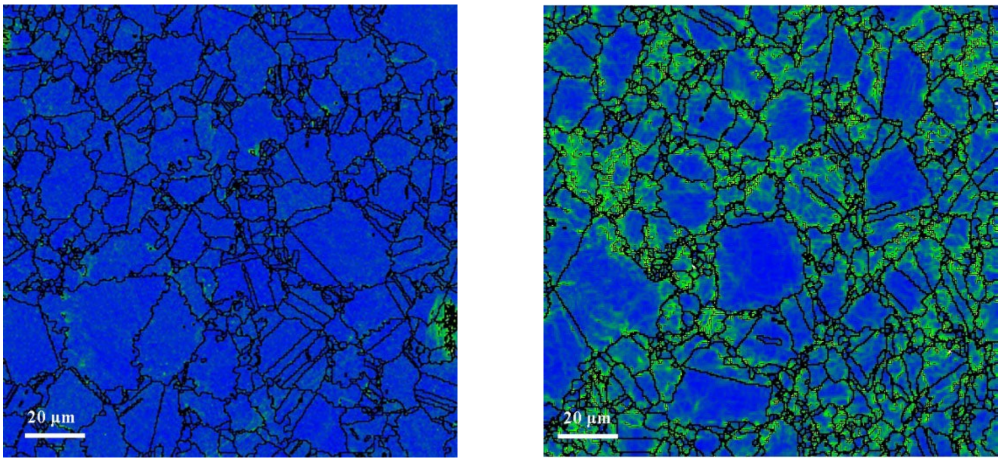

(a)

(b)

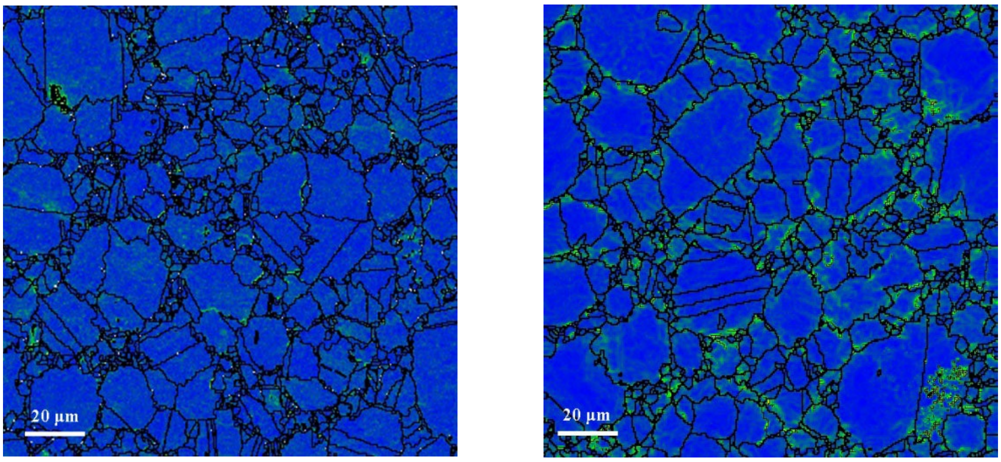

(c) (d)

Figure 13. Local misorientation maps: (a) before creep with 135ppm oxygen content, (b) after creep with 135ppm oxygen content, (c) after creep with 135ppm oxygen content, (d) after creep with 341ppm oxygen content.

3.3. Creep Mechanism

During the creep, dislocations form in the γ matrix and gradually slip to the γ-γ′ phase interface, forming dislocation entanglement gradually. The lattice mismatch stress between γ and γ′ phases can be released by the dislocation entanglement, making dislocations cut through γ′ phase and forming two incomplete dislocations. One of the incomplete dislocations moves along (111) crystal plane to form stacking fault. And finally micro-twins generate [22,23]. Figure 14a shows the micro-twins morphology of FGH96 superalloy with 135ppm oxygen content, which are single directional micro-twins. While Figure 14b displays two directional micro-twins in FGH96 superalloy with 341ppm oxygen content, indicating the cross-slip phenomenon. Therefore, dislocation slip and micro-twins formation is the main creep deformation mechanism of FGH96 superalloy.

However, the slip direction of the original ∑3 boundaries in FGH96 superalloy differentiate form these micro-twins, for which the micro-twins formation and movement will be limited. Consequently, the higher proportion of the ∑3 boundaries in FGH96 superalloy with 135ppm oxygen content slow down the creep rate and contributes a longer creep life. While in FGH96 superalloy with 341ppm oxygen content, multiple directions of slip system motivate simultaneously and slip cross for the weaker resistance by ∑3 boundaries, so the specimen creeped faster and raptured earlier.

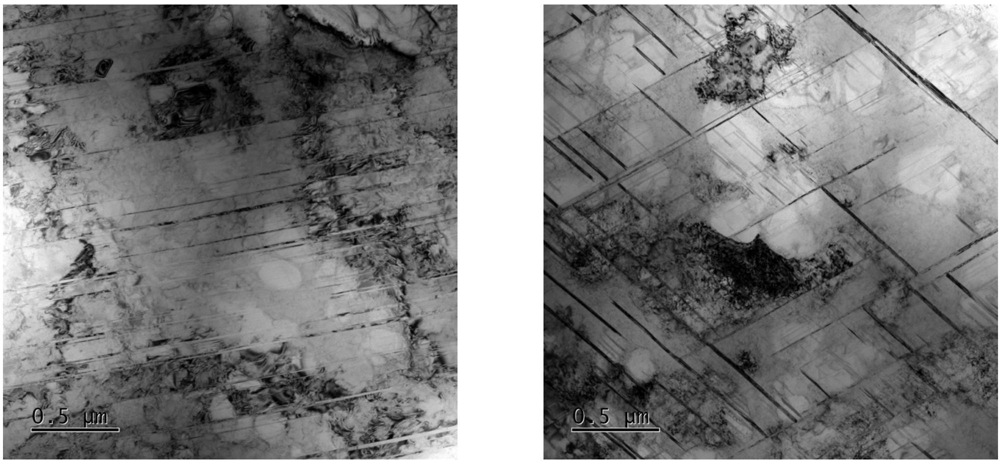

(**a**) (**b**)

Figure 14. TEM images of specimens after creep with different oxygen content: (a) 135ppm, (b) 341ppm.

4. Conclusions

Microstructure and creep property of FGH96 superalloy with different oxygen content were investigated. The major findings are summarized as follows:

1. Oxygen content increased from 135ppm to 341ppm, PPB grade rose from grade 2 to grade 3, and the size of γ' phase on PPB enlarged from 1.07μm to 1.27μm, and MC carbide size grew from 77.4nm to 104.0nm and MC volume fraction increased from 0.15% to 0.22%.
2. Oxygen content increased from 135ppm to 341ppm, steady creep duration shortened from 43h to 21h, and steady creep rate accelerated from 4.34×10^{-3} h^{-1} to 1.87×10-2 h^{-1}, and creep rupture life decreased from 176h to 94h, and the creep rupture mode transferred from intergranular and trans-granular mixed fracture to along PPB fracture.
3. FGH96 superalloy with 341ppm oxygen content has a wider grain size distribution and less ∑3 boundaries compare with lower oxygen content superalloy.
4. Multiple directions of slip system motivate simultaneously and slip cross for the weaker resistance by less ∑3 boundaries in FGH96 superalloy with 341ppm oxygen content, so the specimen creeped faster and raptured earlier.

Acknowledgments: We gratefully thank financial support provided by the National Key Research and Development Program of China, grant number 2021YFB3704000, the National Nature Science Foundation of China, grant number 52071310) and the National Major Science and Technology Project of China, grant number Y2019-VII-0011-0151.

References

1. Thuneman, T.; Raja, K.S.; Charit, I. Room Temperature Corrosion Behavior of Selective Laser Melting (SLM)-Processed Ni-Fe Superalloy (Inconel 718) in 3.5% NaCl Solution at Different pH Conditions: Role of Microstructures. *Crystals* **2024**, *14*, 89.
2. Li, Y.; Zhang, Q.F.; You, X.G.; Qiang, J.B. Effect of Melt Superheating Treatment on the Microstructures and Purity of a Directionally Solidified Superalloy. *Crystals* **2023**, *13*, 1632.
3. Zhang, L.C.; Xu, W.Y. ; Li, Z.; Zheng, L.; Liu, Y.F.; Zhang, G.Q. Characterization of particle shape of nickel-based superalloy powders using image processing techniques. *Powder Technol.* **2022**, *395*, 787-801.
4. Wang, X.Q.; Peng, Z.C.; Luo, X.J.; Hu, H.; Zou, J.W.; Wang, W.X. Effect of aging treatment on microstructure and properties of HEX+HIF FGH95 superalloys. *J. Mater. Eng*. **2020**, *48*, 120-126.
5. Tan, L.M.; He, G.A.; Liu, F.; Li, Y.P.; Jiang, L. Effects of Temperature and Pressure of Hot Isostatic Pressing on the Grain Structure of Powder Metallurgy Superalloy. *Mater.* **2018**, *11*, 328-337.
6. Qiu, C.L.; Attallah, M.M.; Wu, X.H.; Andrews, P. Influence of hot isostatic pressing temperature on microstructure and tensile properties of a nickel-based superalloy powder. *Mater. Sci. Eng. A* **2013**, *564*, 176-185.
7. Ma, W.B.; Liu, G.Q.; Hu, B.F.; Jia, C. Formation of previous particle boundary of nickel base PM superalloy FGH96. *Acta Metall. Sin*. **2013**, *49*, 1248-1254.
8. Zhou, J.Y.; Liu, C.K.; Zhao, W.X.; Zheng, Z.; Zhong, Y. Prior Particle Boundary of PM FGH96 Superalloy and Its In-situ High-cycle Fatigue at Elevated Temperature. *J. Aeron. Mater*. **2017**, *37*, 83-89.
9. Liu, H.S.; Zhang, L.; He, X.B.; Qu, X.H.; Zhu, H.M.; Zhang, G.Q. Effect of oxygen content and heat treatment on carbide precipitation behavior in PM Ni-base superalloys. *Int. J. Min. Metall. Mater*. **2012**, *19*, 827-835.
10. Zhang, L.; Liu, H.S.; He, X.B.; Din, R.; Qu, X.H.; Qin, M.H.; Li, Z.; Zhang, G.Q. Thermal evolution behavior of carbides and γ' precipitates in FGH96 superalloy powder. *Mater. Charact*. **2012**, *67*, 52-64.
11. Zhang, Y.; Zhang, Y.W.; Sun, Z.K.; Huang, H. Influence of PPB on Fatigue Crack Growth Rate of PM Ni - Based Superalloy. *Rare Metal Mat. Eng*. **2019**, *48*, 3282-3288.
12. Rao, G.A.; Srinivas, M.; Satma, D.S. Effect of oxygen content of powder on microstructure and mechanical properties of hot isotatically pressed superalloy Inconel 718. *Mater. Sci. Eng. A* **2006**, *435*, 84-99.
13. He, G.A.; Ding, H.H.; Liu, C.Z.; Liu, F.; Lan, H.; Jiang, L. Effects of powder characteristics on microstructure and deformation activation energy of nickel based superalloy. *Chin. J. Nonferrous Met*. **2016**, *26*, 37-49.
14. MacDonald, J.E.; Khan, R.H.U.; Aristizabal, M.; Essa, K.E.A.; Lunt, M.J.; Attallah, M.M. Influence of powder characteristics on the microstructure and mechanical properties of HIPed CM247LC Ni superalloy. *Mater. Des*. **2019**, *174*, 107796.
15. Tian, T.; Hao, Z.B.; Ge, C.C.; Li, X.; Peng, S.; Jia, C. Effects of stress and temperature on creep behavior of a new third-generation powder metallurgy superalloy FGH100L. *Mater. Sci. Eng. A* **2020**, *776*, 139007.
16. Peng, Z.C.; Liu, P.Y.; Wang, X.Q.; Luo, X.J.; Liu, J.; Zou, J.W. Creep Behavior of FGH96 Superalloy at Different Service Conditions. *Acta Metall. Sin*. **2022**, *58*, 673-682.

17. Xu, H.; Wang, Y.; Liu, D.L.; Zou, J.W. High temperature oxidation resistance of PM superalloys FGH4095 and FGH4096. *J. Mater. Eng*. **2023**, *51*, 122-131.
18. Ingesten, N.G.; Warren, R.; Winberg, L. The Nature and Origin of Previous Particle Boundary Precipitates in P/M Superalloys. Springer Netherlands **1982**, 1013-1027.
19. Zhao, J.P. Study on Prior Particle Boundary (PPB) Precipitation in P/M Superalloy FGH96. Xi'an University of Architecture and Technology, 2010.
20. Xu, W.Y.; Liu, Y.F.; Yuan, H.; Li, Z.; Zhang, G.Q.; Surface Characterization of Nickel-Base Superalloy Powder: Proc. Chin. Mater. Conf. 2018. Springer: Berlin Germany, 2019; pp. 561-567.
21. Peng, Z.C.; Zou, J.W.; Wang, X.Q. Microstructural characterization of dislocation movement during creep in powder metallurgy FGH96 superalloy. *Mater. Today Commun*. **2020**, *25*, 101361.
22. Peng, Z.C.; Zou, J.W.; Yang, J.; Tian, G.F.; Wang, X.Q. Influence of γ' precipitate on deformation and fracture during creep in PM nickel-based superalloy. *Prog. Nat. Sci*. **2021**, *31*, 303-309.
23. Peng, Z.C.; Zou, J.W.; Wang, Y.; Zhou, L.; Tang, Y. Effects of solution temperatures on creep resistance in a powder metallurgy nickel-based superalloy. *Mater. Today Commun.* **2021**, *28*, 102573.